The downward transport of momentum to the surface in idealized sting-jet cyclones

Gwendal Rivière, Didier Ricard, Philippe Arbogast

ORIGINAL ARTICLE

Journal Section

The downward transport of momentum to the surface in idealized sting-jet cyclones

Gwendal Rivière[1] | **Didier Ricard**[2] | **Philippe Arbogast**[3]

[1]LMD/IPSL, École Normale Supérieure, PSL Research University, Sorbonne Université, École Polytechnique, CNRS, Paris, France

[2]CNRM, Université de Toulouse, Météo-France, CNRS, Toulouse, France

[2]Météo-France, Toulouse, France

Correspondence
G. Rivière, LMD/IPSL, Ecole Normale Supérieure, 24 Rue Lhomond, 75231 Paris Cedex 05, France
Email: griviere@lmd.ens.fr

Funding information

Processes leading to the formation of strong surface wind

Abbreviations: SJ, sting jet;

gusts within an idealized sting-jet extratropical cyclone are investigated using a high-resolution mesoscale model. It is motivated by real case studies that have shown that damaging surface winds ahead of the bent-back warm front of an extratropical cyclone are often due to the presence of a sting jet, which is a low-level mesoscale jet whose air masses descend from the cloud head to the top of the boundary layer. Different numerical simulations show that surface winds below the leading edge of the sting jet increase with increased horizontal resolution and surface roughness. For typical land surface roughness, the intensity of the near-surface wind gusts rapidly increases with horizontal resolution while the sting-jet intensity above the boundary layer does not vary with resolution. A focus on the 1-km grid-spacing simulation with land surface roughness is then made. It shows stronger surface winds ahead of the bent-back warm front than near the cold-conveyor-belt jet. It also exhibits multiple bands of strong surface wind speed similarly to real sting-jet cyclones. These multiple bands are closely linked with multiple resolved convective rolls in the boundary layer whose descending branches are responsible for the downward transfer of momentum. Sensitivity experiments and a stability analysis show that the cooling due to sublimation and melting of precipitating ice hydrometeors below the leading edge of the sting jet trigger and invigorate the boundary-layer convective rolls by reducing the buoyancy of air masses near the precipitation base and below. Closer to the surface, the transfer of momentum is predominantly taken over by subgrid-scale turbulent fluxes.

KEYWORDS
Sting-jet, wind, gust, bent-back warm front, convective rolls, evaporating precipitation

1 | INTRODUCTION

Damaging surface winds inside extratropical cyclones may happen in different regions relative to the cyclones center and may originate from different dynamical processes. Moderate to strong winds may occur ahead of the cold front

along the warm conveyor belt when the cyclone develops toward its mature stage (Browning and Pardoe, 1973; Grønås, 1995; Lackmann, 2002). Another source of strong winds is the cold-conveyor-belt jet (CCBJ) in the vicinity of the warm front as it wraps cyclonically around the cyclone center (Carlson, 1980; Browning, 1990; Schultz, 2001). At a later stage, in the so-called Shapiro-Keyser cyclone types (Shapiro and Keyser, 1990), damaging winds may occur southwestward of the cyclone center along the cold conveyor belt (CCB) or south of the cyclone center ahead of the CCB in the presence of a sting jet (hereafter denoted as SJ; see Figs. 1, 2 of Hewson and Neu, 2015; Hart et al., 2017; Schultz and Browning, 2017, for an illustration). The SJ phenomenon has been introduced by Browning (2004) when studying the Great Storm of October 1987 that led to huge damages in northwest France and southeast England. The SJ is a mesoscale jet above the CCB jet associated with air masses descending from the cloud head in the midtroposphere to the top of the boundary layer. Then, boundary-layer processes help to transfer high momentum down to the surface. Most studies on SJ analyzed real wind storms in the North Atlantic sector (Clark and Gray, 2018) but this does not mean that it does not occur in other storm-track regions. For instance, a recent paper by Brâncus et al. (2019) showed the occurrence of a SJ in a Mediterranean extratropical cyclone. Very few studies directly observed SJs or their effects at the surface. Parton et al. (2009) observed the detailed vertical structure of the SJ of windstorm *Jeanette*, thanks to the VHF wind profiler at Aberystwyth. Direct airborne in-situ measurements of SJ were made during the DIAMET campaign for Friedhelm storm (Baker et al., 2013; Martinez-Alvarado et al., 2014a; Vaughan et al., 2015). The CCB jet and SJ were shown to merge in some regions even though the associated air streams had different origins. More recently, 1-minute resolution wind measurements made with the Chibolton Doppler radar provided information on the downward transfer of momentum from the SJ toward the surface in the St-Jude storm (Browning et al., 2015).

There are no climatologies of directly detected SJs and very few climatologies of SJ precursors exist. The resolution of models producing reanalysis data being too coarse to represent mesoscale jets like sting jets only indirect information on the existence of SJ can be provided through the detection of large-scale precursors (Martinez-Alvarado et al., 2012; Hart et al., 2017). The first climatology by Martinez-Alvarado et al. (2012) (see also Martinez-Alvarado et al., 2014b) showed that a third of 100 intense storms in the North Atlantic exhibited SJ precursors. This proportion was confirmed by the more extensive climatology from Hart et al. (2017) based on seasons from 1979 to 2012 with a slightly greater percentage found for explosively developing cyclones than nonexplosively developing cyclones. Also, SJ cyclones represent 42% of the population of explosively cyclones and half of the strong wind cyclones crossing the British Isles. A recent study by Martinez-Alvarado et al. (2018) showed that the number of cyclones exhibiting the sting-jet precursors increases from 32% to 45% between present-day and future climate simulations under the most extreme climate-change scenario.

Most existing studies on SJs investigated mechanisms for the formation of SJs. Since SJ air masses exhibit slantwise descending motions, the release of conditional symmetric instability (CSI Bennetts and Hoskins, 1979; Schultz and Schumacher, 1999) was first hypothesized to play a key role in these motions by Browning (2004). Since then, different diagnostics have been applied to check the relevance of CSI such as the downdraft slantwise convective available potential energy (Gray et al., 2011) or the saturated moist potential vorticity (Martinez-Alvarado et al., 2010; Baker et al., 2014; Martinez-Alvarado et al., 2014a; Coronel et al., 2016; Volonté et al., 2018). Most studies found evidence of unstable conditions for CSI within the cloud head in the upstream region of the descending SJ air masses (Gray et al., 2011; Baker et al., 2014; Martinez-Alvarado et al., 2014a; Volonté et al., 2018), and Volonté et al. (2018) also showed evidence of unstable conditions for symmetric and inertial instabilities. Coronel et al. (2016) identified neutral conditions for CSI in their idealized SJ cyclones but this could be the signature of already released CSI according to Clark and Gray (2018). It is likely that real SJ cyclones exist without being strongly unstable to CSI (Smart and Browning, 2014; Clark and Gray, 2018). Another branch of studies made an emphasis on the role played by balanced dynamics. Regions of SJ descents are co-located with geostrophically-forced descending motions as diagnosed by the divergence

of the Q-vector (Coronel et al., 2016; Slater et al., 2017) and could be in large part connected to the frontolytic descent in the SJ region (Schultz and Sienkiewicz, 2013; Slater et al., 2015, 2017). The strong horizontal wind speed occurring in the co-located regions of the CCB jet and SJ southwest and south of a Shapiro-Keyser cyclone are mainly due to the along-flow pressure gradient force (Slater et al., 2015) or equivalently the pressure work (Rivière et al., 2015b). A third potential mechanism is the evaporative cooling that could reinforce both the SJ descent and horizontal wind speed but idealized and more realistic simulations showed that its effect is rather weak (Baker et al., 2014; Coronel et al., 2016; Smart and Browning, 2014). The review paper by Clark and Gray (2018) concluded that there is a continuum of mechanisms explaining the presence of SJ in which the balanced descents associated with synoptic-scale dynamics can be reinforced by mesoscale moist instabilities like CSI.

One aspect which has been less studied is the dynamics of downward transfer of high momentum from the sting jet to the surface (Clark and Gray, 2018). Strong surface winds between the head of the bent-back warm front and the cold front might be due to the presence of the CCB jet or SJ or both (Smart and Browning, 2014). Analyzing satellite imagery from Meteosat, Browning and Field (2004) identified different arc-shaped and chevron-shaped clouds within the boundary layer of the Great Storm of October 1987 suggesting the presence of boundary-layer convergence lines ahead of the downward transport of momentum. Most studies showed that regions of strong surface winds below SJs were collocated with regions of weak boundary-layer static stability. For instance, Clark et al. (2005) found that below SJs, the wet-bulb potential temperature was quite constant leading to neutral conditions for moist convection. In another context, Kelley et al. (2019) showed that the momentum of an elevated jet of a lee cyclone can be brought down to the surface where the static stability below is neutral to unstable. However, in most places, the top of the boundary layer just below SJs is characterized by enhanced static stability as seen in observed cases (Browning and Field, 2004) and idealized cases (Baker et al., 2014; Coronel et al., 2016). What is happening near the top of the boundary layer in a region of strong vertical shear is still unclear (Clark and Gray, 2018). Within the boundary layer, ahead of the bent-back warm front, the static stability is probably reduced compared to other regions which seems to favor the transfer of momentum by convective rolls (Clark et al., 2005; Schultz and Sienkiewicz, 2013; Browning et al., 2015; Hewson and Neu, 2015; Slater et al., 2017). In their study of the St-Jude storm, Browning et al. (2015) identified different convective cells some of them being shallow and confined in the boundary layer, some others being more elevated. They also emphasize the importance of evaporative precipitation residues and showers in bringing down high momentum to the surface. Finally, Slater et al. (2017) showed how surface fluxes destabilize the boundary layer and help transferring momentum down to the surface. The present study aims at investigating processes responsible for the downward transfer of momentum within the same idealized framework as that of Coronel et al. (2016) which does not contain any surface fluxes.

In order to simulate idealized sting jets, it is necessary to get a bent-back warm front which is likely to form in cyclones crossing the slowly-varying large-scale jet (Rivière et al., 2015a,b; Coronel et al., 2016). It also requires enough horizontal and vertical resolutions. A 10-km grid-spacing simulation is usually enough to represent SJs and most numerical studies have used this kind of resolution (see table 3 of Clark and Gray, 2018). An appropriate ratio between the vertical and horizontal grid spacings of about 1/50 were also mentioned to be the key to correctly simulate SJ and their associated slantwise descending motions (Persson and Warner, 1993; Lean and Clark, 2003; Clark et al., 2005). However, in Coronel et al. (2016), this ratio was not found to be crucial once the horizontal resolution is high enough. Only three studies have looked at better horizontal grid spacing than 10 km: 7-km in Martinez-Alvarado et al. (2010), 5-km in Smart and Browning (2014) and 4-km in Coronel et al. (2016). In the present study, we will decrease the grid spacing to 1 km. The aim is to resolve boundary-layer convective rolls of few kilometers similar to those described for the St-Jude storm by Browning et al. (2015).

The paper is organized as follows. The model and setup of the simulations are presented in section 2. Section 3 is

dedicated to the results. It includes analysis of sensitivity experiments for which the horizontal grid spacing and surface roughness are changed. The way high momentum is transferred downward is analyzed by computing passive tracers and by separating the downward momentum fluxes into subgrid-scale and resolved components. The effect of evaporative cooling is then studied by turning off this process in one simulation. Finally, instability criteria facilitating mixing are computed such as the Richardson number and the criterion for cloud-base detrainment instability. A summary of the results is provided in section 4.

2 | METHOD

2.1 | Model

The model used to simulate the idealized SJ cyclone is the non-hydrostatic mesoscale research model Meso-NH (Lafore et al., 1998; Lac et al., 2018). It has the same configuration as in Coronel et al. (2016). It includes the one-moment bulk-cloud microphysical scheme ICE3 of Pinty and Jabouille (1998) with five prognostic hydrometeors (cloud droplets, rain, ice crystals, snow and graupel mixing ratios, in addition to water vapour). Subgrid-scale transports are parametrized by the mass-flux scheme for deep convection of Bechtold et al. (2001) and a 1.5-order closure scheme for turbulence (Cuxart et al., 2000) with the turbulence mixing length formulation of Bougeault and Lacarrère (1989). Surface conditions are specified at the lower boundary with a prescribed roughness length. There is no radiation scheme, the surface sensible and latent heat fluxes are set to zero and the shallow convection scheme is disabled.

2.2 | Set up of simulations

The model domain is 10 000 km long in the zonal direction and 6000 km wide in the meridional direction (Figure 1(a)). The vertical extension is 16 km. Zonal boundaries are cyclic and the northern and southern boundaries have wall boundary conditions. The vertical resolution has an irregular vertical level spacing and increases with altitude. It is fixed for all simulations of the present study and corresponds to 50-150 m spacing between the ground and 2 km altitude, 150-290 m between 2 and 5 km altitude and 290–430 m between 5 and 8 km.

A 20-km grid-spacing simulation is first performed over the whole domain up to $t = 96$ h starting from the same initial conditions as those shown in Figure 1 of Coronel et al. (2016). The simulation is denoted S20sea_parent and its state at $t = 72$ h is used to initialize the other simulations described in the present paper (Figure 1(a)). S20sea_parent has a roughness length of 2×10^{-4} m corresponding to a typical value for sea surface. The initial flow consists of a zonal baroclinic jet and two synoptic-scale disturbances located near the tropopause and the surface. The jet axis is located halfway between the southern and northern boundaries and the two disturbances are located south of the jet axis which is a favorable condition to form a Shapiro-Keyser cyclone (Rivière et al., 2015a,b). During their evolution, the two disturbances baroclinically interact with each other and the zonal jet. A deep surface cyclone forms, crosses the jet axis and reaches a maximum deepening of about 940 hPa once located north of the jet axis after 3 to 4 days (Figure 1(a)).

Two sets of three simulations with 20-km, 4-km and 1-km grid spacings are then performed. Only the 20-km grid-spacing simulation uses the mass-flux scheme for deep convection as convective motions are explicitly resolved for the 4-km and 1-km grid-spacing simulations. For the first set, the roughness length is 2×10^{-4} m corresponding to typical sea surface. The associated three simulations are respectively called S20sea, S4sea and S1sea. S20sea and S4sea are initialized with the S20sea_parent state at $t = 72$ h (Figure 1(a)) and last until $t = 96$ h. S20sea is run over the large domain and S4sea over the red square domain shown in Figure 1(a). The red square domain is chosen to include the mature stage of the cyclone during which a SJ is formed and the seclusion stage occurs (Coronel et al., 2016). The

TABLE 1 List of simulations

Simulations	grid spacing	Roughness	Suppressed processes	two-way nesting
S20sea_parent	20 km	0.0002	none	no
S20sea	20 km	0.0002	none	yes
S4sea	4 km	0.0002	none	yes
S1sea	1 km	0.0002	none	yes
S20land	20 km	0.01	none	yes
S4land	4 km	0.01	none	yes
S1land	1 km	0.01	none	yes
S1land_nocl	1 km	0.01	no evaporative cooling from precipitation	yes
S1land_nocl_noevap	1 km	0.01	no evaporative cooling and no evaporation	yes

interactions between the S20sea and S4sea simulations is made using a two-way nesting, meaning that both simulations run at the same time and exchange information in both directions, to obtain the most accurate state for S4sea. S20sea and S4sea are the same as the low-high and high-high resolution simulations discussed in Coronel et al. (2016). S1sea is performed from $t = 84$ h to 96 h and nested in the domain shown by the black square in Figure 1. To get S1sea, a 20-km grid spacing run is performed over the whole domain, interacting with a 4-km grid-spacing run in the red domain, which itself interacts with a 1-km grid spacing run in the black domain from $t = 84$ h to 96 h. The latter run is called S1sea.

Exactly the same procedure is applied for the second set of 20-km, 4-km and 1-km grid-spacing simulations for which the roughness length is set to 10^{-2} m corresponding to a typical smoothed land surface. The runs are respectively called S20land, S4land and S1land and are performed in the same domains as S20sea, S4sea and S1sea, respectively. The choice of the 1-km grid spacing domain is such that it includes the southern part of the cyclone during the time interval between $t = 84$ h and 96 h. During that time interval, the domain contains a low-level jet above the boundary layer at $z = 2$ km that moves from the southwest to the south of the cyclone center, that is, between the leading edge of the bent-back warm front and the cold front (Figures 1(b),(c)). This low-level jet has been identified as being a SJ in Coronel et al. (2016). Indeed, backward trajectories starting from the wind maximum at $z = 1.8$ km to the south of the cyclone center at $t = 96$ h confirm that the air masses have undergone rapid descending motions from the cloud head situated at $z = 3.5$ km with increased wind speed and dryness.

A last set of two simulations is performed in the black square domain from $t = 84$ h to 96 h. S1land_nocl is the same simulation as S1land but for which the evaporative cooling from precipitating hydrometeors (rain, graupel, and snow) is turned off but the conversion into vapour is allowed to happen. S1land_nocl_noevap is the same simulation as S1land but both the evaporative cooling and evaporation transition are suppressed. Table 1 summarizes all the experiments analysed in the present paper.

3 | RESULTS

3.1 | Resolution effects and roughness effects

Figure 2 shows the horizontal wind speed above the boundary layer at $z = 1.6$ km and the cloud structure at $t = 93$ h for S20land, S4land and S1land. The SJ extends from the west to the south of the cyclone center and reaches a maximum

value of about 42 m s^{-1} at $x = 8400$ km, $y = 3000$ km for the three simulations. A secondary maximum of the SJ is also visible for the three simulations near the cloud head with values around 37 m s^{-1}. To conclude on Figure 2, there is no major difference in the amplitude and location of the SJ between the different horizontal grid spacings. As noticed in Coronel et al. (2016), differences appear when the vertical grid is too coarse and the structure of the SJ disappears for a 500-m vertical grid spacing.

Near the surface, at $z = 25$ m, a local maximum of horizontal wind speed of about 23 m s^{-1} appears below the maximum wind speed of the SJ and CCB jet at roughly $x = 8450$ km, $y = 3100$ km for all resolutions (Figures 3(a),(c),(e)). This maximum is located 100 km southwest of the bent-back warm front. More downstream, for the 20-km grid spacing, the wind speed continuously decreases (Figure 3a) whereas for the 4-km and 1-km grid spacings, bands of wind speed maxima appear in a region of weak thermal contrasts around $x = 8900$ km (Figures 3(c),(e)). For the 1-km grid spacing, wind speed maxima in these bands reach values as high as 26 m s^{-1} which is stronger than the upstream maximum near the bent-back warm front.

The different bands of wind speed maxima for S4land and S1land have a rather barotropic structure in the boundary layer. They correspond to descending air masses starting a bit below the SJ, which is located around $z = 1.5$ km, and finish near the surface. These descending regions are separated by ascending ones with local wind speed minima (Figures 3(d),(f)). In S1land, the alternating resolved ascents and descents have typical intensities of about 0.5 m s^{-1} and typical wavelength of 5-20 km. The correlation between the vertical velocity and the horizontal wind speed in the region where these bands of wind speed maxima appear and inside the boundary layer is rather high: it varies between 0.6 and 0.8 depending on the region. In S4land, the ascents and descents are 2 to 3 times weaker than in S1land and the typical wavelength is about 20 km or larger. In S20land, some bands of wind speed maxima are only slightly visible and their associated vertical motions are much weaker than for the other two simulations (this is the reason why no contour appears in Figure 3b). The peaks of vertical motions in S20land are roughly 3 times smaller than those of S4land. To conclude on the land surface roughness simulations, the intensity of the near-surface wind gusts below the leading edge of the sting jet rapidly increases with horizontal resolution while the sting-jet intensity above the boundary layer does not vary with resolution.

For the simulations with typical sea surface roughness (Figure 4), the multiple near-surface wind speed maxima farther ahead of the bent-back warm front are less intense and much less visible than those with typical land roughness. For S20sea (Figures 4(a),(b)), they are almost absent; for S4sea they start to appear (Figures 4(c),(d)) and for S1sea (Figures 4(e),(f)) they are visible but less intense than for S1land. On the contrary, the maximum along the CCB jet near $x = 8400$ km, $y = 3100$ km is greater for S20sea, S4sea and S1sea than for S20land, S4land and S1land and reaches values close to 32 m s^{-1} as a result of a weaker friction near the surface. The SJ is also stronger for sea surface roughness than land surface roughness, about 40 m s^{-1} for the former and 36 m s^{-1} for the latter along the cross section AA'. Another interesting difference is that along the same cross section, the CCB jet is still visible for sea roughness simulations and not at all for land surface simulations. Finally, even though S1sea exhibits alternating bands of local maxima and minima in wind speed along AA', the maxima are still significantly weaker than the large-scale maximum along the CCB jet.

For all simulations performed with a sea surface roughness, the global maximum wind speed found at the surface was along the CCB jet and not farther ahead of it as in Coronel et al. (2016). It is only in the case of the 1-km grid-spacing simulation with land roughness that maxima ahead of the CCB jet are stronger than the maximum located along the CCB jet. Both the resolution and the roughness are responsible for setting the maximum wind speed in the region of weak thermal contrasts between the head of the bent-back warm front and the cold front.

The evolution of multiple bands of near-surface wind speed maxima for S1land is shown in Figure 5 between $t = 91$ h and $t = 96$ h. Between $t = 91$ h and $t = 93$ h (Figures 5(a)-(f)), many bands such as those inside or near the yellow squares

are located below the leading edge of the SJ at $z = 1.6$ km. Some others are more to the northeast of the SJ main core region as those located in the domain $x = 8800–8900$ km and $y = 2900–3000$ km at $t = 91.5$ h (Figure 5(b)). They also appear below high values of wind speed at $z = 1.6$ km but the values are weaker than below the SJ main core region. We noticed that on its northeastern flank the SJ is very thin in the vertical direction and peaks around $z = 1.5$ km. This small vertical extension is well visible in Figure 3(f) close to A' between $y = 2900$ km and $y = 3000$ km while the SJ is deeper and more intense south of $y = 2900$ km. So most of the bands of wind speed maxima are found below the leading edge of the SJ but not necessarily where the sting jet is the strongest. Between $t = 94$ h and $t = 96$ h (Figures 5(g)-(i)), small-scale bands of near-surface wind speed maxima appear roughly 100 km upstream of the previously described ones (see e.g., near $x = 8700$ km $y = 2850$ km at $t = 94$ h). These newly created bands appear below the leading edge of another wind speed maximum at the SJ level ($z = 1.6$ km) which is visible in the figure from $t = 92$ h. Between $t = 92$ h and $t = 96$ h, we clearly see two large-scale wind speed maxima within the SJ region: the first bands of near-surface wind speed maxima are located below the first SJ maximum while the second bands below the leading edge of the second SJ maximum. The origins of these two types of bands are hereafter analyzed.

3.2 | The distinct role of subgrid-scale and resolved circulations in downward transfer of momentum

To check that part of the air masses reaching the surface is indeed coming from the sting jet, passive tracers are initialized from $t = 90$ h to $t = 93$ h at the grid point $x = 8550$ km $y = 2800$ km and its 8 adjacent neighbours between $z = 1.5$ km and 2.0 km. This grid point was chosen by using backward Lagrangian trajectories starting at $t = 93$ h in the free troposphere just above a particular near-surface wind speed maximum at $x = 8920$ km $y = 2820$ km (not shown). Figure 5 shows the evolution of the passive tracer at the level of the SJ ($z = 1.6$ km). At $t = 91$ h, the leading edge of the green contour is in a region of maximum wind speed of the SJ while at $t = 93$ h it is more ahead of it. The eastward advection of the passive tracer is thus faster than the displacement of the SJ wind speed maxima.

Figure 6 exhibits a zoom of the evolution of the passive tracer. At $t = 91$ h (Figure 6(a)), there is no trace of the passive tracer in the boundary layer. At $t = 91.5$ h, a first pinch of passive tracer appears in the middle of the boundary layer around $x = 8690$ km $y = 2790$ km (see blue shadings in Figure 6(b)). The passive tracer content entering the boundary layer locally increases with time as seen around $x = 8740$ km $y = 2795$ km at $t = 92$ h (Figure 6(c)) and $x = 8770$ km $y = 2800$ km at $t = 92.25$ h (Figure 6(d)). Downstream of this peak in passive tracer content, one can easily see a local maximum in horizontal wind speed at $z = 200$ m located around $x = 8720$ km $y = 2790$ km at $t = 91.5$ h, $x = 8775$ km $y = 2800$ km at $t = 92$ h and $x = 8800$ km $y = 2805$ km at $t = 92.25$ h. This maximum increases with time between $t = 91.5$ h and $t = 92$ h and then keeps constant until $t = 93$ h.

At $t = 92.25$ h (Figure 6(d)), a second pinch of passive tracer enters the middle of the boundary layer at $x = 8810$ km $y = 2800$ km in connection with a local wind speed maximum located more downstream. Fifteen minutes later (Figure 6(e)), this new intrusion of passive tracer forms a long zonal band extending from $x = 8790$ km to $x = 8860$ km which terminates into two small branches, one near the previously mentioned wind speed maximum at $x = 8850$ km $y = 2805$ km and a more intense wind speed maximum at $x = 8880$ km $y = 2805$ km. The latter maximum slightly increases with time from $t = 91.5$ h to $t = 92.5$ h (Figures 6(b)-(e)) and then slightly decreases between $t = 92.5$ h and $t = 93$ h (Figures 6(e)-(f)). All the intrusions of passive tracer within the boundary layer move more rapidly to the north than the passive tracer at the top of the boundary layer because of more intense northward winds within the boundary layer than at the top (not shown).

Figure 7 shows different vertical cross sections at $t = 92.5$ h in the region of the second burst of downward transport of passive tracer to identify key processes allowing such a downward transport. The cross section xx' is made along the

main direction of the wind in the boundary layer and has been chosen in such a way that it crosses the near-surface wind maximum located around x=8880 km y=2805 km. Above this near-surface wind maximum, a peak value of downward momentum fluxes is well visible and located below the edge of high passive tracer content at the top of the boundary layer (Figure 7(b)). Some passive tracer content has been transported downward by this cell of downward motion but the amount of passive tracer transported to the surface is rather small: the ratio between the peaks at the surface and those at the sting jet level is of the order of a few percent (see blue contours in Figure 7). The peak values of passive tracer near the surface are located upstream of the near-surface wind maximum. This can be explained by the fact that the eastward displacement of the passive tracer at the SJ level (roughly $z = 1.5$ km) is more rapid than the eastward displacement of the convective rolls of the boundary layer. Once the high passive tracer content at the SJ level reached a cell of downward motion, the passive tracer starts to descend at the western edge of the descending cell. A bit later, the high passive tracer content at the SJ level covers the whole descending cell and there is therefore more passive tracer content at the western edge of the descending cell than at the eastern edge. This explains why the peak in passive tracer content near the surface appears behind the descending cell in Figure 7(b). The same observations can be made when looking at the latitudinal cross sections of Figures 7(c)-(e): the passive tracer is just starting to descend in the most eastern section (cc') while it is already much closer to the surface in the most western section (aa'). In the latitudinal cross sections, the downward intrusion of passive tracer is better co-located with the intense downward momentum fluxes than in section xx' (Figure 7(b)) because the bands of downward motion are longitudinally oriented and the flow is mainly zonal. However, there is a slight northward shift of the passive tracer content relative to the downward motion in the latitudinal cross sections (aa'), (bb') and (cc') because there are slightly more northward winds inside the boundary layer compared to the top as noticed in the previous paragraph. In all cross sections, a good co-location of regions of high wind speed and downward momentum fluxes in the boundary layer is seen. Finally, turbulent fluxes are more active very near the surface where they are homogeneously oriented downward and reach values as large as the resolved fluxes below z=500 m (see shadings in Figure 7(a)). The comparison between the black contours of Figures 7(a) and (c), which represent the resolved and total momentum fluxes respectively, shows that the subgrid-scale fluxes have a significant contribution to the downward transfer of momentum in the first hundred meters of the atmosphere only.

To better quantify the relative roles of the resolved and subgrid-scale fluxes, Figure 8 shows their average in two distinct regions of the boundary layer at $t = 92.5$ h, one located near the bent-back warm front (pink square in Figure 5(e)) and the other further downstream below the leading edge of the SJ (yellow square in Figure 5(e)). The averages are made in these two regions only where the horizontal wind speed near the surface ($z = 200$ m) exceeds 28 m s^{-1} in order to focus on the downward transport of high momentum. In the downstream region, such a selection leads to a wind profile with a peak near $z = 400$ m as seen in the red curve of Figure 8(a). In the downstream region, the subgrid-scale fluxes are an order of magnitude smaller than the resolved ones at altitude higher than 300 m. Below 300 m, the resolved fluxes become smaller and smaller closer to the surface while the subgrid-scale fluxes become more and more intense. In that region, it is only in the last 50 m above the surface that the subgrid-scale fluxes dominate in the downward transport of momentum. In the upstream region, the wind profile monotonically increases with height in the boundary layer (red curve in Figure 8(b)) and the amplitude of the resolved momentum fluxes is seven times as small as the same quantity in the downstream region. Because the resolved fluxes are much less intense in the upstream region and because the subgrid-scale fluxes are stronger at higher altitude, the role played by the latter fluxes is relatively more important in the upstream region than in the downstream one. The sum of the two fluxes, corresponding to the total transport of momentum, is much larger in the downstream region than in the upstream one because of the large difference in the resolved fluxes. This explains why there is higher momentum closer to the surface in the downstream region despite a weaker SJ there (compare the red curves in Figures 8(a),(b)).

To conclude, at the leading edge of the SJ, the downward transfer of momentum occurs sporadically through bursts

of resolved downward circulations starting near the top of the boundary layer. In the lowest part of the boundary layer, below 100 m of altitude, it mainly occurs through subgrid-scale turbulent fluxes.

3.3 | Effect of evaporative cooling from precipitating hydrometeors

As mentioned in the introduction, the role of evaporative cooling in the intensity of the descent and horizontal wind speed of the SJ has been quantified in the idealized simulations of Baker et al. (2014) and Coronel et al. (2016) by turning off the evaporative cooling. In both cases, the impact was shown to be negligible or small. For instance, the effect does not exceed 2 m s^{-1} within the core of the SJ. Evaporative cooling process has also been hypothesized to be the key process for the downward transfer of momentum from the SJ down to the surface by Browning et al. (2015). The idea is that evaporative cooling of precipitation residues could decrease the buoyancy of air masses near the top of the boundary layer and help the air masses to descend and bring down high momentum all the way to the surface. Figure 9(b) shows that precipitation maxima occur in regions of local minima of horizontal wind speed at the top of the boundary layer at $z = 1.0$ km, in agreement with Vaughan et al. (2015). However, closer to the surface, the peaks in precipitation gets closer to the peaks of wind speed as seen for instance at $z = 0.5$ km from abscissa 180 to 220 km. The role of evaporative cooling of these precipitation residues in the wind acceleration nearby is questioned.

To test the hypothesis of the role of evaporative cooling in the downward transport of momentum inside the boundary layer, S1land_nocl has been performed in which the evaporative cooling from precipitating hydrometeors (rain, snow, graupel) has been turned off at $t = 84$ h. Since the sum of snow and graupel largely dominates over rain, the suppressed cooling is mainly due to the sublimation and melting of solid precipitation. The impact is indeed quite large in the bands of maximum wind speed near the cloud head at the boundary-layer level. Almost all the bands of wind gusts of about 32–36 m s^{-1} located along a moderate-intensity near-surface cold front are suppressed (see the axis BB' in Figures 9(a),(b) and compare with Figures 9(c),(d)). The cold front disappears in that region and the temperature is more homogeneous when the evaporative cooling of precipitating hydrometeors is turned off (compare the black contours in Figures 9(a) and (c)). The sensitivity run S1land_nocl clearly shows that evaporative cooling of the leading edge of the boundary-layer cloud head and its associated precipitation is an important process for the formation of multiple bands of wind gusts. On the contrary, the wind speed maximum within the CCB jet increases by up to 2-4 m s^{-1} (upper-left quadrant of Figures 9(a),(c)). Suppressing the evaporative cooling tends to reinforce the depression (the SLP minimum is 2 hPa lower in S1land_nocl than in S1land) and the winds to the southwest of the cyclone center in the CCB region. There is also a long band of strong wind gust near $x = 8700$ km, $y = 2920$ km that exist in S1land_nocl and not in S1land. So the suppression of evaporative cooling does not prevent the formation of bands of strong wind gusts but almost entirely suppresses those located at the leading edge of the boundary-layer cloud filaments.

In the simulation where the evaporative cooling is suppressed and the evaporation is prevented (S1land_nocl_noevap), precipitation cannot evaporate and therefore reach the ground as seen in Figure 9(f). In that case, the bands of wind gusts along the axis BB' are less numerous than in S1land but do not completely disappear in contrast with S1land_nocl (compare Figures 9(a) and (e)). Regions where these bands disappear are those located further away from the maximum wind speed of the sting jet, around $x = 8650$–8800 km and $y = 2650$–2750 km (see Figures 5(f) and 9(a),(b)). More upstream, in the CCB region, surface wind gusts in S1land_nocl_noevap are weaker than in S1land_nocl but slightly stronger than in S1land. The comparison between S1land_nocl_noevap and S1land_nocl indicates that the newly created water vapor via evaporation helps intensifying the winds below the CCB jet but prevents the downward transfer of momentum from the sting jet to the surface at the leading edge of the cloud. The boundary layer is also warmer in S1land_nocl than in S1land_nocl_noevap, especially near the top of the boundary layer (not shown), because it leaves the possibility for the newly created water vapor via evaporation to condense once again.

To conclude, the effect of the evaporating precipitation below the leading edge of the sting jet is twofold. On the one hand, the evaporative cooling itself tends to strongly invigorate the convective rolls within the boundary layer. On the other hand, the newly formed water vapor via evaporation, which can condense once again, acts to diminish the intensity of the rolls. The first effect overwhelms the second effect and the net effect of evaporating precipitation is to multiply the number of convective rolls in the boundary layer and hence to reinforce the downward transfer of momentum at the leading edge of the sting jet. Further insights on the evaporative cooling effect is provided in next section.

3.4 | Richardson number, static stability and cloud-base detrainment instability

To determine why the downward transport of high momentum is more efficient below the leading edge of the sting jet than more upstream, different quantities have been computed and shown in Figures 10 and 11. The strategy is first to look at $t = 90$ h (Figure 10) when convective rolls start to be formed. Three types of quantities are computed to detect favorable conditions for turbulence and instabilities: (i) the Richardson number (or its bulk formula) which provides information on turbulence and mixing activity when it is positive and small and on convective stability when it is negative, (ii) the static stability parameter which more directly provides information on convective instability (iii) a criterion satisfying the cloud-base detrainment instability (CDI) as initially proposed by Emanuel (1981). As shown hereafter, these quantities closely depend on the cooling effect on the buoyancy associated with the sublimation and melting of precipitating ice hydrometeors.

Figure 10(a) shows the Bulk Richardson number $Ri_B = (g/T_v)(\Delta\theta_v \Delta z)/((\Delta u)^2 + (\Delta v)^2)$ computed at $t = 90$ h in S1land between $z = 0.1$ km and $z = 1.2$ km, where g is the gravitational acceleration, T_v is the virtual temperature, $\Delta\theta_v$ is the virtual potential temperature difference across the chosen layer of thickness $\Delta z = 1.1$ km, and Δu and Δv are the changes in horizontal wind components across that same layer. The time $t = 90$ h has been chosen because it is just prior to the occurrence of the convective rolls and we want to check what are the favorable environmental conditions triggering the rolls. A zone of relatively low values of Ri_B appears below the leading edge of the SJ in the area limited by $x = 8600$–8800 km and $y = 2700$–2900 km. This area also corresponds to the separation area between high ice water content (sum of cloud ice, snow and graupel) (zone with green asterisks) and low ice water content. This region of relatively weak Ri_B is due to lower values of the static stability parameter there and not due to stronger shear. Stronger shears are found in another region more upstream in the vicinity of the bent-back warm front. Therefore, the variations of the static parameter dominates over that of the shear in the Bulk Richardson number of S1land. There is also a region of rather low values of Ri_B below the leading edge of the SJ in S1land_nocl (Figure 10(d)) but it is less well localized than in S1land and extends further upstream.

Vertical cross sections YY' are made inside the area of low values of Ri_B (Figures 10(b),(d)). They show the local Richardson number ($Ri = N_v^2/|\partial \mathbf{u}/\partial z|^2$ with $N_v^2 = (g/\theta_v)(\partial\theta_v/\partial z)$) in shadings and the zone of high ice water content (sum of cloud ice, snow and graupel mixing ratios) in green contour. The lower interface between high ice water content and no ice water content is hereafter called the precipitation base because it corresponds to a strong gradient of the sum of snow and graupel mixing ratios. For S1land, Ri is always negative from the precipitation base to the surface (Figure 10(b)), due to negative static stability parameter N_v^2. There are some exceptions where convective cells have already formed at $y = 2720$ km and $y = 2840$ km. The negative values appearing below the precipitation base can be attributed to the cooling associated with the sublimation and melting of precipitating solid hydrometeors. This is shown by comparing with S1land_nocl (Figure 10(e)). In a layer of 200 m depth below the precipitation base, Ri is systematically positive in S1land_nocl and only becomes negative closer to the surface. The effect of cooling by sublimation and melting of precipitation on the static stability was confirmed by looking at S1land_nocl_noevap which does not present strong

negative values of static stability below the precipitation base because the evaporative cooling is turned off in that simulation too. The reason why S1land_nocl_noevap presents more convective rolls than S1land_nocl (see Figures 9(c),(e)) might be due to the slightly more negative values of static stability found in the former run compared to the latter (not shown). Indeed, the newly formed water vapor via sublimation, can condense again and warm the air masses. Such a warming was found to be more important near the top of the boundary layer which has the effect of stabilizing the boundary layer in S1land_nocl compared to S1land_nocl_noevap.

Farther upstream, along the cross section ZZ', the high values of ice water content are found at a lower altitude due to a lower cloud base and lower precipitating hydrometeors (Figures 10(c),(f)). The low values of Ri are only found in a limited layer close to the surface in both runs. However, S1land presents negative values just below the high values of ice water content while S1land_nocl still presents positive values there. As above, this reflects the effect of evaporative cooling of precipitating hydrometeors in S1land.

Another mechanism for vertical destabilization of the air masses below the leading edge of the sting jet could be the destabilization of cloud-base air masses via cloud-base detrainment instability (CDI) as initially introduced by Emanuel (1981) to explain mammatus formation. CDI corresponds to an instability of the interface between cloudy air above and subsaturated air below. Mixing triggers the instability by bringing cloudy air into the subsaturated environment below and the condensate inside the mixed air is evaporated or sublimated. The associated cooling effect helps to decrease the buyoancy of the air masses that then extend their descent. Kanak et al. (2008) showed that the CDI criterion is necessary to form mammatus and that the sublimation of ice is a key process to get mammatus in their simulations. Even though the considered scales are larger in the present case, the configuration is similar with the leading edge of the cloud base overlying a region of rather low humidity in the boundary layer. The CDI criterion has been applied here as in Kanak et al. (2008) for ice clouds because liquid contents are small compared to solid contents in the present case. We define the ice water virtual potential temperature as

$$\theta_{iv} = T_v \left(\frac{p_0}{p}\right)^{\chi} \left(1 - \frac{q_i}{1+q_t}\right) \left(1 - \frac{q_i}{0.622+q_t}\right)^{\chi-1} \left(1 - \frac{q_i}{q_t}\right)^{-\gamma} \exp\left(\frac{-L_s q_i}{(C_p + q_t C_{pv})T}\right), \tag{1}$$

and

$$\chi \equiv \frac{R_d + R_v q_t}{C_p + C_{pv} q_t}, \tag{2}$$

$$\gamma \equiv \frac{R_v q_t}{C_p + C_{pv} q_t}. \tag{3}$$

The ice water virtual potential temperature corresponds to the virtual potential temperature an air parcel would have if all ice in the parcel were sublimated. q_v is the water mixing ratio, $q_i = q_{snow} + q_{ice} + q_{graupel}$ is the ice water content, sum of all ice species, q_{snow} is the snow mixing ratio, q_{ice} is the cloud-ice mixing ratio and $q_t = q_v + q_i$ is the sum of all mixing ratios (kg kg^{-1}). L_s is the latent heat of sublimation (J kg^{-1}), T is the temperature (K), C_p is the heat capacity at constant pressure for dry air (J kg^{-1} K^{-1}), C_{pv} is the heat capacity at constant pressure of vapor (J kg^{-1} K^{-1}), R_d is the gas constant of dry air, R_v is the gas constant of water vapor, p_0 is the reference pressure and p is the pressure. Following Emanuel (1994, p220-221) and Kanak et al. (2008) the CDI criterion can be expressed as

$$\Delta\theta_{iv} = (\theta_{iv})_c - (\theta_{iv})_e < 0, \tag{4}$$

where c and e refers to the cloud and clear air below the cloud, respectively. In the present case, the criterion is applied everywhere as follows

$$\theta_{iv}(z + \Delta z/2) - \theta_{iv}(z - \Delta z/2) < 0, \qquad (5)$$
$$q_i(z + \Delta z/2) > 5\,10^{-3}\,\mathrm{g\,kg^{-1}},$$

where $\Delta z/2 \simeq 100$ m is the approximate level spacing of the simulations in the boundary layer. The regions where the criterion is satisfied are shown in yellow shadings in Figures 10(b),(c),(e),(f). The two simulations clearly show that at $t = 90$ h, the CDI criterion is met at the precipitation base. Such a criterion has been applied with the total ice content, that is, with q_i being equal to the sum of cloud ice, snow and graupel mixing ratios. If the same computation is made by replacing q_i by the cloud ice mixing ratio only (not shown), the areas satisfying the CDI criterion entirely disappear. It confirms that the precipitating hydrometeors and their sublimation are the key for the destabilization of the air masses. In that sense, the CDI criterion in the present study cannot be thought as corresponding to the instability of the cloud base air masses only as it is closely related to the presence of precipitating hydrometeors.

Since variations of the Richardson number are dominated by fluctuations of the static stability in the region of interest, Figure 11 shows the static stability parameter. It is computed in two ways: one is N_v^2 (Figures 11(a),(c)) and the other $N_{iv}^2 = (g/\theta_{iv})(\partial\theta_{iv}/\partial z)$ (Figures 11(a),(c)). For S1land, N_v^2 is positive above the precipitation base and negative from the precipitation base down to the surface. In contrast, for S1land_nocl, it is positive in a layer of few hundred meters below the precipitation base. As already mentioned, it reveals the cooling effect of sublimating hydrometeors. The main difference between N_v^2 and N_{iv}^2 occurs at the precipitation base where the latter is negative. This corresponds to the yellow areas of Figure 10 and highlight the potential instability the air masses have if some precipitation is mixed with the more subsaturated air and sublimate. In other words, the negative values of N_v^2 below the precipitation base correspond to the cooling of precipitation that happened before $t = 90$ h while the negative values of N_{iv}^2 at the precipitation base correspond to the potential cooling effect of precipitation that may occur after $t = 90$ h. In S1land_nocl, negative values of N_{iv}^2 also appear at the precipitation base and the CDI criterion is also satisfied in that region. However, since the sublimation cooling is suppressed in that simulation, the instability cannot be released.

At $t = 93$ h, once the convective cells have fully developed, the CDI criterion is almost not satisfied in the downstream vicinity of the cells (see cross section in Figure 12(b) and compare to the one shown in Figure 10(b)) and the static stability is not homogeneously negative anymore. It suggests that the first round of convective rolls have consumed the instabilities. At the same time, the CDI criterion is met more upstream of the first round of cells near the new cross section ZZ' (Figures 12(a),(c)). As mentioned earlier and shown in Figures 5(g),(h),(i), after $t = 93$ h, a second round of convective cells appear. Therefore, our analysis suggests that the CDI and the convective instability below help to destabilize the air below the leading edge of the SJ first but also farther upstream at later times. This could explain the occurrence of the two clusters of convective cells.

To conclude, the criteria for CDI at the precipitation base and convective instability below the precipitation base are satisfied before the occurrence of the convective cells and disappear once they are fully mature, suggesting that the instabilities are consumed. Both instabilities are set by the cooling effect of sublimation and melting of snow and graupel hydrometeors. These sublimation and melting processes more easily happen, and the instabilities are more easily satisfied, at the leading edge of the sting jet because it is the region marked by advection of cloudy air above subsaturated air. It is still not clear if sublimation and melting of precipitating hydrometeors is triggered by mixing as required in the CDI theory. In that case, the mixing could be initiated because of the weak positive values of the Richardson number at the precipitation base. Another possibility is that sublimation and melting naturally occur once the precipitation falls into the subsaturated air.

4 | CONCLUSION

The present study investigates processes leading to the formation of maximum surface wind gusts within an idealized sting-jet cyclone simulated with the mesoscale model Meso-NH. A focus is made on surface wind gusts appearing between the head of the bent-back warm front and the cold front in a region of weak thermal contrasts. Different numerical simulations performed at different horizontal grid spacings with different surface roughness values show that surface winds ahead of the bent-back warm front and below the leading edge of the sting jet increase by increasing both the horizontal resolution and the surface roughness. For a given surface roughness, the intensity of these surface winds increases with resolution while the sting-jet intensity above the boundary layer stays almost the same. Only the 1-km grid-spacing simulation with typical land surface roughness (S1land) exhibits stronger surface winds ahead of the bent-back warm front than near the cold-conveyor-belt jet. For coarser resolution and/or weaker roughness, the maximum surface wind gusts occur below the cold-conveyor-belt jet.

The downward transfer of momentum in the boundary layer of the S1land simulation is organized by along wind convective rolls where the maximum surface wind gusts are correlated with the descending branches of the convective rolls . The correlation varies between 0.6 and 0.8 depending on the regions. Also, at the top of the boundary layer peaks in precipitation correspond to minima of horizontal wind speed and are co-located with the upper part of the ascending branches of the rolls. The distance between two consecutive bands of maximum surface winds typically varies between 5 km and 10 km. The S1land simulation rather adequately reproduces the multiple bands of strong surface wind speed reported in the literature for sting-jet cyclones. For instance, it brings similarities with the "St-Jude" or "Christian" storm studied by Browning et al. (2015) even though the spacing between the individual bands of maximum wind speed was found to be smaller for the real storm (between 500 m and 3 km).

Passive tracers initiated in the SJ region were computed to better understand how the momentum is transferred to the surface. The tracer can stay for few hours in the vicinity of the SJ near the top of the boundary layer without being transferred further downward. But once the descending branch of a convective roll approaches the region of high passive tracer content, a rapid downward transfer happens and in almost half an hour some passive tracer content is transported from the top of the boundary layer to the surface. Therefore, these are the resolved convective rolls that initiate and transport the tracer until reaching a few hundred meters above the surface. Then, the turbulent fluxes take over the downward transport of tracer and momentum in the last hundred meters of the atmosphere. More upstream, closer to the bent-back warm front, such convective activity is almost absent and the downward transfer of momentum much less efficient and less localized.

Then, the paper addressed the question of why such downward transfer of momentum by convective rolls happen below the leading edge of the sting jet in the vicinity of the head of the boundary-layer clouds. Before the formation of the convective rolls in S1land, we show this region is marked by low values of the Bulk Richardson number computed between the top of the boundary layer and the surface. These low values are not related to greater values of the wind shear but rather to lower values of the static stability. The static stability presents negative minima just below the precipitation base and stays negative down to the surface. Such a feature is identified as being due to the cooling due to sublimation and melting of snow and graupel near and below the cloud base. This is confirmed by turning off the cooling associated to these processes in a sensitivity experiment. In that simulation, the convective rolls completely disappear and the static stability is slightly positive in the few hundred meters below the precipitation base. It confirms that evaporating precipitation, mostly sublimation in the present case, is a key process for the downward transfer of momentum inside the boundary layer as suggested by Browning et al. (2015). It is also in good agreement with the role of evaporation in facilitating convection in the boundary layer as described in Browning and Smart (2018) in a different context. An analysis of the cloud-base detrainment instability (CDI) has been also performed showing that

the CDI criterion is satisfied before the occurrence of the convective cells and largely disappear once the cells are well formed, suggesting that the instability is consumed after a while. However, the CDI criterion has been applied to the sum of all ice species and such an instability is not satisfied in the present case by considering cloud ice only. The instability comes from the potential sublimation of snow and graupel. In that sense, it cannot be strictly seen as a pure cloud-base destabilization as precipitation must be taken into account. In the simulation where the evaporative cooling of precipitating hydrometeors is turned off, the CDI criterion is still satisfied but the instability cannot be released because it precisely requires sublimation and melting of ice. Our conclusion is that before the occurrence of the convective rolls, both criteria for CDI at the precipitation base and convective instability in the subsaturated air below are satisfied. Conditions for convective instability below the precipitation base are met because there was a cooling due to sublimation and melting of solid precipitation that led to that condition. Conditions for CDI at the precipitation base are met because there is the potential for subsequent cooling as soon as precipitation will be mixed with the subsaturated air below. Hence, our interpretation is that the convective rolls are formed by destabilization of the air masses at the precipitation base via CDI and the associated air masses continue their descent because they met favorable conditions for convective instability further below the precipitation base.

The present study provides new insights on the boundary-layer processes responsible for the downward transfer of momentum from the sting jet to the surface. One nice result is that it provides guidance of how to form multiple bands of strong surface winds below the leading edge of the sting jet in an idealized numerical set up. The two key identified parameters are horizontal resolution and surface roughness. We also show that, with a very simple setup of the boundary layer, it is possible to trigger mixing and downward transport of momentum just by destabilization of air masses from the top of the boundary layer. This strong vertical mixing by convective rolls was found in different observational studies (e.g., Parton et al., 2009; Browning et al., 2015) but not well represented or absent in simulations of real cases (Parton et al., 2009) or in simulations of idealized cases (Baker et al., 2014; Coronel et al., 2016). In the present study, we were able to represent this strong vertical mixing by convective plumes in our model and to identify the dominant processes that help to form such intense convective plumes. These are mainly the sublimation and melting of precipitating ice hydrometeors. We also show that, even though a 10–15 km horizontal grid spacing with a 200–300 m level spacing is enough to represent sting jets themselves (Clark and Gray, 2018), much higher resolution is required to accurately represent the downward transfer of momentum inside the boundary layer. The next step will be to consider a more realistic boundary layer that will include surface fluxes of heat and moisture by imposing a forcing by sea surface temperature. This will destabilize the boundary layer from below and this will also facilitate the downward transfer of momentum as shown in the real case study of Slater et al. (2017).

ACKNOWLEDGEMENTS

This work has been supported by the French national programme LEFE/INSU. The authors would like to acknowledge Suzanne Gray for fruitful discussions on various occasions over the course of this study and in particular for her suggestion of using passive tracers. We thank the two reviewers, David Schultz and an anonymous one, for their helpful comments that allowed us to significantly improve the paper.

REFERENCES

Baker, L., Gray, S. L. and Clark, P. A. (2014) Idealised simulations of sting-jet cyclones. *Quart. J. Roy. Meteor. Soc.*, **140**, 96–110.

Baker, L., Martinez-Alvarado, O., Methven, J. and Knippertz, P. (2013) Flying through extratropical cyclone friedhelm. *Weather*, **68**, 9–13.

Bechtold, P., Bazile, E., Guichard, F., Mascart, P. and Richard, E. (2001) A mass flux convection scheme for regional and global models. *Quart. J. Roy. Meteor. Soc.*, **127**, 869–886.

Bennetts, D. and Hoskins, B. J. (1979) Conditional symmetric instability - a possible explanation for frontal rainbands. *Quart. J. Roy. Meteor. Soc.*, **105**, 945–962.

Bougeault, P. and Lacarrère, P. (1989) Parameterization of orography-induced turbulence in a mesobeta–scale model. *Mon. Wea. Rev.*, **117**, 1872–1890.

Brâncus, M., Schultz, D. M., Antonescu, B., Dearden, C. and Stefan, S. (2019) Origin of strong winds in an explosive mediterranean extratropical cyclone. *Mon. Wea. Rev.*, **147**, 3649–3671.

Browning, K. A. (1990) *Organization of clouds and precipitation in extratropical cyclones*, vol. : extratropical cyclones, Erik Palmén memorial volume, chap. 8, 129–153. American Meteorological Society.

— (2004) The sting at the end of the tail: Damaging winds associated with extratropical cyclones. *Quart. J. Roy. Meteor. Soc.*, **130**, 375–399.

Browning, K. A. and Field, M. (2004) Evidence from meteosat imagery of the interaction of sting jets with the boundary layer. *Meteor. Appl.*, **11**, 277–289.

Browning, K. A. and Pardoe, C. (1973) Structure of low-level jet streams ahead of mid-latitude cold fronts. *Quart. J. Roy. Meteor. Soc.*, **99**, 619–638.

Browning, K. A. and Smart, D. J. (2018) Invigoration of convection by an overrunning diabatically modified cloud-top layer. *Quart. J. Roy. Meteor. Soc.*, **144**, 142–155.

Browning, K. A., Smart, D. J., Clark, M. R. and Illingworth, A. J. (2015) The role of evaporating showers in the transfer of sting-jet momentum to the surface. *Quart. J. Roy. Meteor. Soc.*, **141**, 2956–2971.

Carlson, T. (1980) Airflow through midlatitude cyclones and the comma cloud pattern. *Mon. Wea. Rev.*, 1498–1509.

Clark, P. A., Browning, K. and Wang, C. (2005) The sting at the end of the tail: Model diagnostics of fine-scale three-dimensional structure of the cloud head. *Quart. J. Roy. Meteor. Soc.*, **131**, 2263–2292.

Clark, P. A. and Gray, S. L. (2018) Sting jets in extratropical cyclones: a review. *Quart. J. Roy. Meteor. Soc.*, **144**, 943–969.

Coronel, B., Ricard, D., Rivière, G. and Arbogast, P. (2016) Cold-conveyor-belt jet, sting jet and slantwise circulations in idealized simulations of extratropical cyclones. *Quart. J. Roy. Meteor. Soc.*, **182**, 1781–1796.

Cuxart, J., Bougeault, P. and Redelsperger, J. L. (2000) A turbulence scheme allowing for mesoscale and large-eddy simulations. *Quart. J. Roy. Meteor. Soc.*, **126**, 1–30.

Emanuel, K. A. (1981) A similarity theory for unsaturated downdrafts within clouds. *J. Atmos. Soc.*, **38**, 1541–1557.

— (1994) *Atmospheric convection*. Oxford University Press. 580 pp.

Gray, S. L., Martinez-Alvarado, O., Baker, L. H. and Clark, P. A. (2011) Conditional symmetric instability in sting-jet storms. *Quart. J. Roy. Meteor. Soc.*, **137**, 1482–1500.

Grønås, S. (1995) The seclusion intensification of the New Year's day storm 1992. *Tellus*, **47A**, 733–746.

Hart, N., Gray, S. and Clark, P. (2017) Sting-jet windstorms over the North Atlantic: climatology and contribution to extreme wind risk. *J. Climate*, **30**, 5455–5471.

Hewson, T. and Neu, U. (2015) Cyclones, windstorms and the imilast project. *Tellus A*, **67**, 27128.

Kanak, K. M., Straka, J. M. and Schultz, D. M. (2008) Numerical simulation of mammatus. *J. Atmos. Sci.*, **65**, 1606–1621.

Kelley, J. D., Schultz, D. M., Schumacher, R. and Durran, D. R. (2019) Can mountain waves contribute to damaging winds far away from the lee slope ? *Wea. Forecasting*.

Lac, C., Chaboureau, P., Masson, V., Pinty, P., Tulet, P., Escobar, J., Leriche, M., Barthe, C., Aouizerats, B., Augros, C., Aumond, P., Auguste, F., Bechtold, P., Berthet, S., Bieilli, S., Bosseur, F., Caumont, O., Cohard, J.-M., Colin, J. M., Couvreux, F., Cuxart, J., Delautier, G., Dauhut, T., Ducrocq, V., Filippi, J.-B., Gazen, D., Geoffroy, O., GHEUSI, F., Honnert, R., Lafore, P., Lebeaupin Brossier, C., Libois, Q., Lunet, T., Mari, C., Maric, T., Mascart, P., Mogé, M., Molinié, G., Nuissier, O., Pantillon, F., Peyrillé, P., Pergaud, J., Perraud, E., Pianezze, J., Redelsperger, J.-L., Ricard, D., Richard, E., Riette, S., Rodier, Q., Schoetter, R., Seyfried, L., Stein, J., Suhre, K., Taufour, M., Thouron, O., Turner, S., Verrelle, A., Vié, B., Visentin, F., Vionnet, V. and Wautelet, P. (2018) Overview of the Meso-NH model version 5.4 and its applications. *Geoscientific Model Development Discussions*, 1929–1969.

Lackmann, G. (2002) Cold-frontal potential vorticity maxima, the low-level jet, and moisture transport in extratropical cyclones. *Mon. Wea. Rev.*, 59–74.

Lafore, J.-P., Stein, J., Asencio, N., Bougeault, P., Ducrocq, V., Duron, J., Fischer, C., Héreil, P., Mascart, P., Masson, V., Pinty, J.-P., Redelsperger, J. L., Richard, E. and de Arellano, J. V.-G. (1998) The meso-nh atmospheric simulation system. part i: adiabatic formulation and control simulations. *Ann. Geophysicae*, **16**, 90–109.

Lean, H. W. and Clark, P. A. (2003) The effects of changing resolution on mesocale modelling of line convection and slantwise circulations in fastex iop16. *Quart. J. Roy. Meteor. Soc.*, **129**, 2255–2278.

Martinez-Alvarado, O., Baker, L. H., Gray, S. L., Methven, J. and Plant, R. S. (2014a) Distinguishing the cold conveyor belt and sting jet airstreams in an intense extratropical cyclone. *Mon. Wea. Rev.*, **142**, 2571–2595.

Martinez-Alvarado, O., Gray, S., Hart, N., P.A. Clark, K. H. and Roberts, M. (2018) Increased wind risk from sting-jet windstorms with climate change. *Environ. Res. Lett.*, **13**, 044002.

Martinez-Alvarado, O., Gray, S. L., Catto, J. L. and Clark, P. A. (2012) Sting jets in intense winter north-atlantic windstorms. *Environ. Res. Lett.*, **7**, 024014, doi: 10.1088/1748–9326/7/2/024014.

— (2014b) Corrigendum: Sting jets in intense winter north-atlantic windstorms (2012 environmental research letters 7, 024014). *Environ. Res. Lett.*, **9**, 039501, doi: 10.1088/1748–9326/9/3/039501.

Martinez-Alvarado, O., Weidle, F. and Gray, S. L. (2010) Sting jets in simulations of a real cyclone by two mesoscale models. *Mon. Wea. Rev.*, **138**, 4054–4075.

Parton, G., Vaughan, G., Norton, E. G., Browning, K. A. and Clark, P. A. (2009) Wind profiler observations of a sting jet. *Quart. J. Roy. Meteor. Soc.*, **135**, 663–680.

Persson, P. O. G. and Warner, T. T. (1993) Nonlinear hydrostatic conditional symmetric instability: Implications for numerical weather prediction. *Quart. J. Roy. Meteor. Soc.*, **121**, 1821–1833.

Pinty, J.-P. and Jabouille, P. (1998) A mixed-phase cloud parameterization for use in a mesoscale non-hydrostatic model: Simulations of a squall line and of orographic precipitations, in paper presented at conference on cloud physics, *Am. Meteorol. Soc., Everett, WA.* 217–220.

Rivière, G., Arbogast, P. and Joly, A. (2015a) Eddy kinetic energy redistribution within idealized extratropical cyclones using a two-layer quasi-geostrophic model. *Quart. J. Roy. Meteor. Soc.*, **141**, 207–223.

— (2015b) Eddy kinetic energy redistribution within windstorms *Klaus* and *Friedhelm*. *Quart. J. Roy. Meteor. Soc.*, **141**, 925–938.

Schultz, D. (2001) Reexamining the cold conveyor belt. *Mon. Wea. Rev.*, 2205–2225.

Schultz, D. and Browning, K. A. (2017) What is a sting jet ? *Weather*, **72**, 63–66, doi: 10.1002/wea.2795.

Schultz, D. and Sienkiewicz, J. (2013) Using frontogenesis to identify sting jets in extratropical cyclones. *Wea. Forecasting*, **28**, 603–613.

Schultz, D. M. and Schumacher, P. N. (1999) The use and misuse of conditional symmetric instability. *Mon. Wea. Rev.*, **127**, 2709–2732, Corrigendum 128: 1573.

Shapiro, M. and Keyser, D. (1990) *Fronts, jet streams and the tropopause*, vol. Extratropical cyclones, Newton and Holopainen eds, chap. 10, 167–191. American Meteorological Society.

Slater, T., Schultz, D. and Vaughan, G. (2015) Acceleration of near-surface strong winds in a dry, idealized extratropical cyclone. *Quart. J. Roy. Meteor. Soc.*, **141**, 1004–1016.

— (2017) Near-surface strong winds in a marine extratropical cyclone: acceleration of the winds and the importance of surface fluxes. *Quart. J. Roy. Meteor. Soc.*, **143**, 321–332.

Smart, D. and Browning, K. (2014) Attribution of strong winds to a cold conveyor belt and sting jet. *Quart. J. Roy. Meteor. Soc.*, **140**, 595–610.

Vaughan, G., Methven, J. and co authors (2015) Cloud banding and winds in intense European cyclones: Results from the DIAMET project. *Bull. Amer. Meteor. Soc.*, **96**, 249–265.

Volonté, A., Clark, P. A. and Gray, S. L. (2018) The role of mesoscale instabilities in the sting-jet dynamics of windstorm *tini*. *Quart. J. Roy. Meteor. Soc.*, **144**, 877–899.

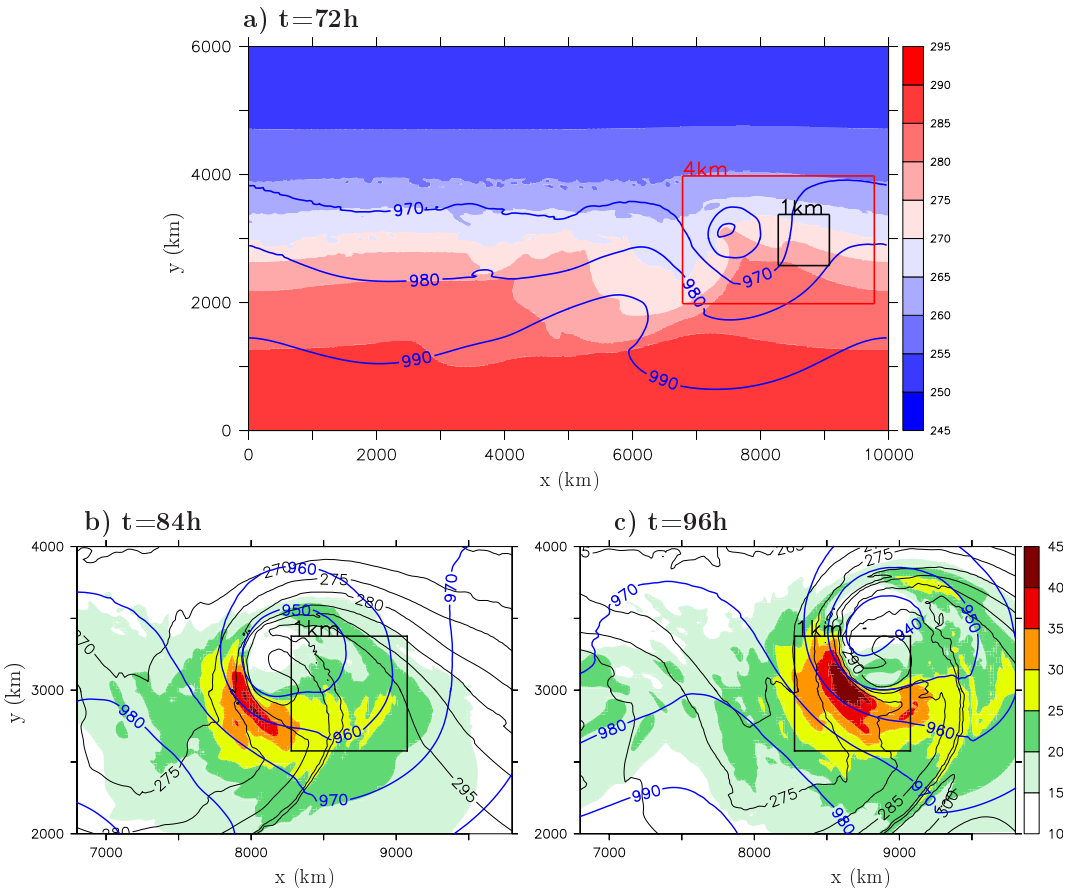

FIGURE 1 (a) Initial state of S20land, S20sea, S4land, S4sea experiments: the temperature field at $z = 25$ m is represented in shadings (units: K), the pressure at $z = 25$ m in blue contours (interval: 10 hPa). (b),(c) Horizontal wind speed at $z = 1.6$ km (shadings; units: m s^{-1}), sea level pressure (blue contours; interval: 10 hPa), and equivalent potential temperature at $z = 1.6$ km (black contours; interval: 5 K) for the simulation S20land for (a) $t = 84$ h and (b) $t = 96$ h. The black square corresponds to the domain of the 1-km grid spacing simulations.

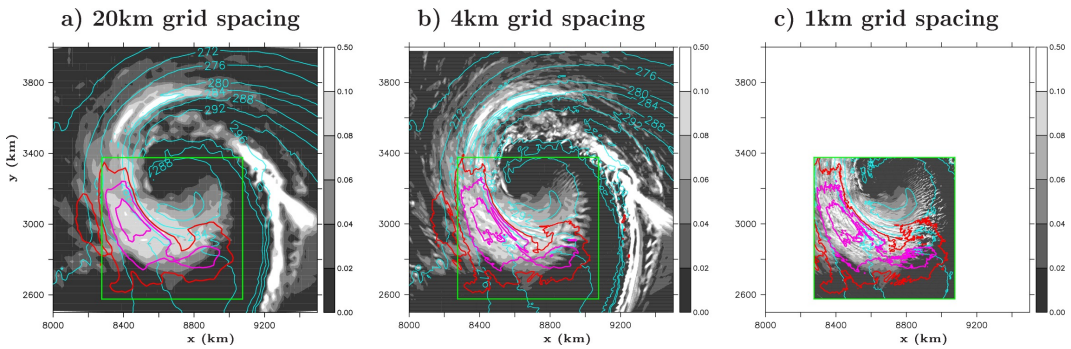

FIGURE 2 Maximum of the sum of cloud liquid and ice water contents between $z = 0.5$ km and $z = 2.0$ km (grey shadings; units: g kg^{-1}), horizontal wind speed at $z = 1.6$ km (30 m s^{-1} in red and 35 and 40 m s^{-1} in magenta), and equivalent potential temperature at $z = 1.6$ km (light blue contours; interval: 4 K) at $t = 93$ h for different simulations: (a) S20land, (b) S4land and (c) S1land.

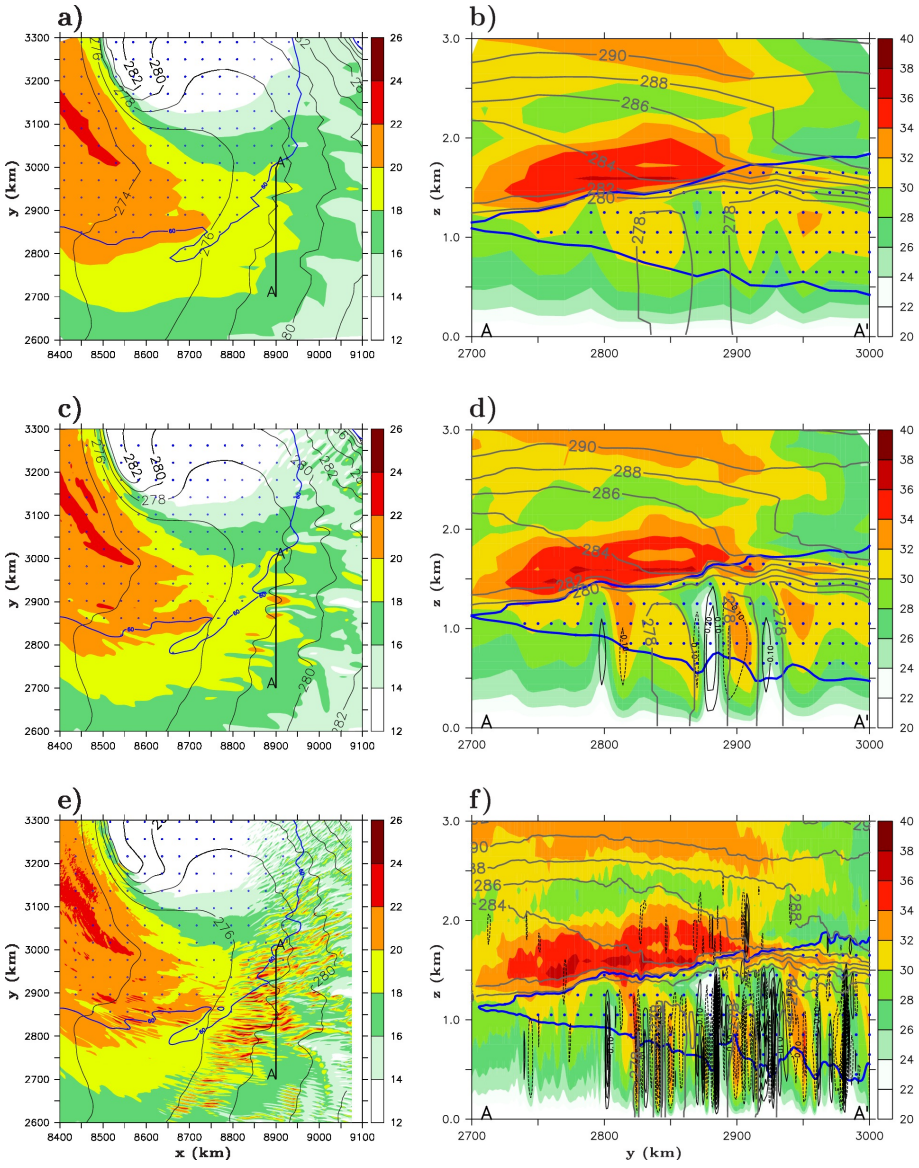

FIGURE 3 (Left column) Horizontal wind speed (shadings; units: m s^{-1}), relative humidity greater than 60% (blue contour and stippled areas), and equivalent potential temperature at $z = 25$ m (black contour; interval: 2 K) at $t = 93$ h. The latter two fields are smoothed for the 4-km and 1-km grid-spacing simulations but not the wind speed. (Right column) Vertical cross section of the horizontal wind speed (shadings; units: m s^{-1}), 80% relative humidity (blue contour), equivalent potential temperature (magenta contour; interval: 2 K) and vertical velocity (black dashed and solid contours for negative and positive values respectively; interval: 0.1 m s^{-1}). Simulations with land roughness: (upper panels) S20land, (middle panels) S4land and (lower panels) S1land.

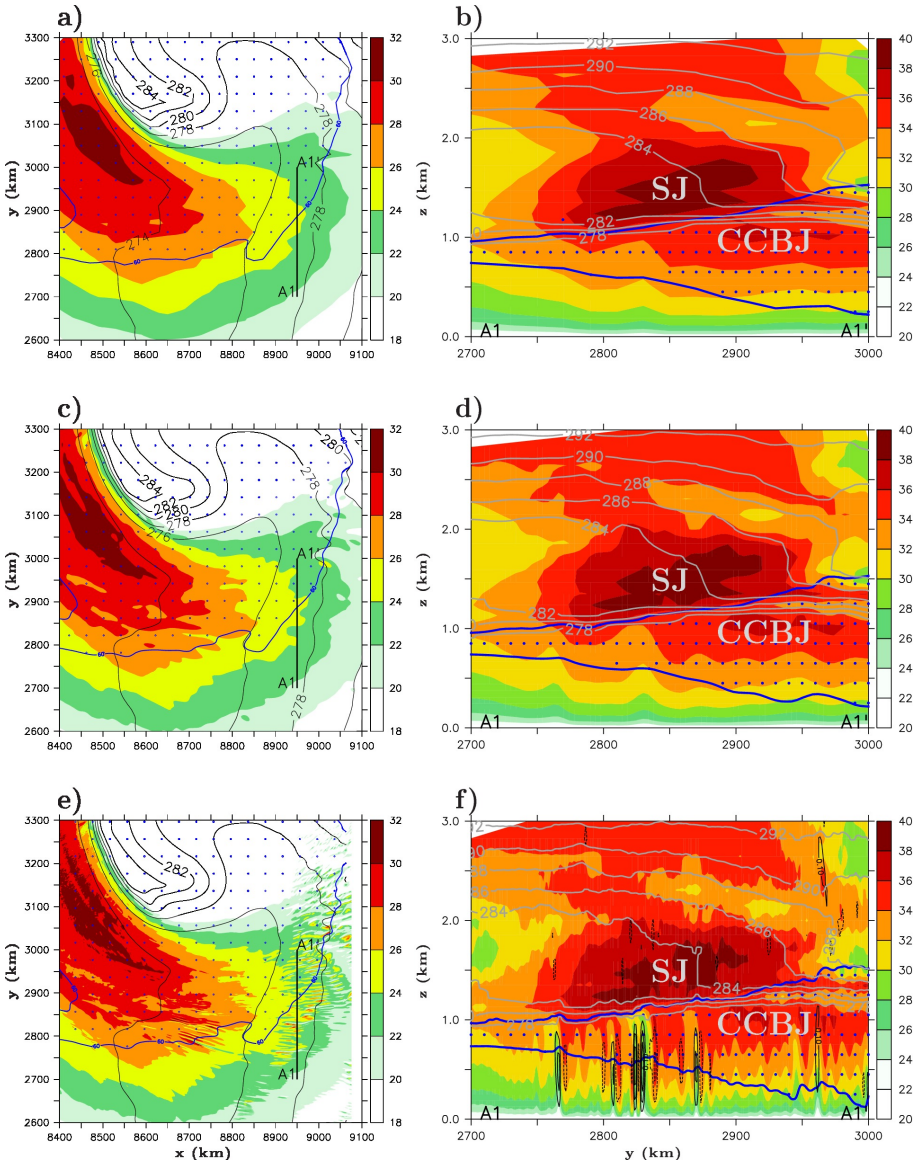

FIGURE 4 Same as Figure 3 but for simulations with sea surface roughness: (upper panels) S20sea, (middle panels) S4sea and (lower panels) S1sea. Note that the vertical cross sections A1A1' are 50 km ahead of the vertical cross sections AA' shown in Figure 3 to select the small-scale bands of near-surface wind speed maxima. SJ and CCBJ correspond to the sting jet and cold-conveyor-belt jet locations, respectively.

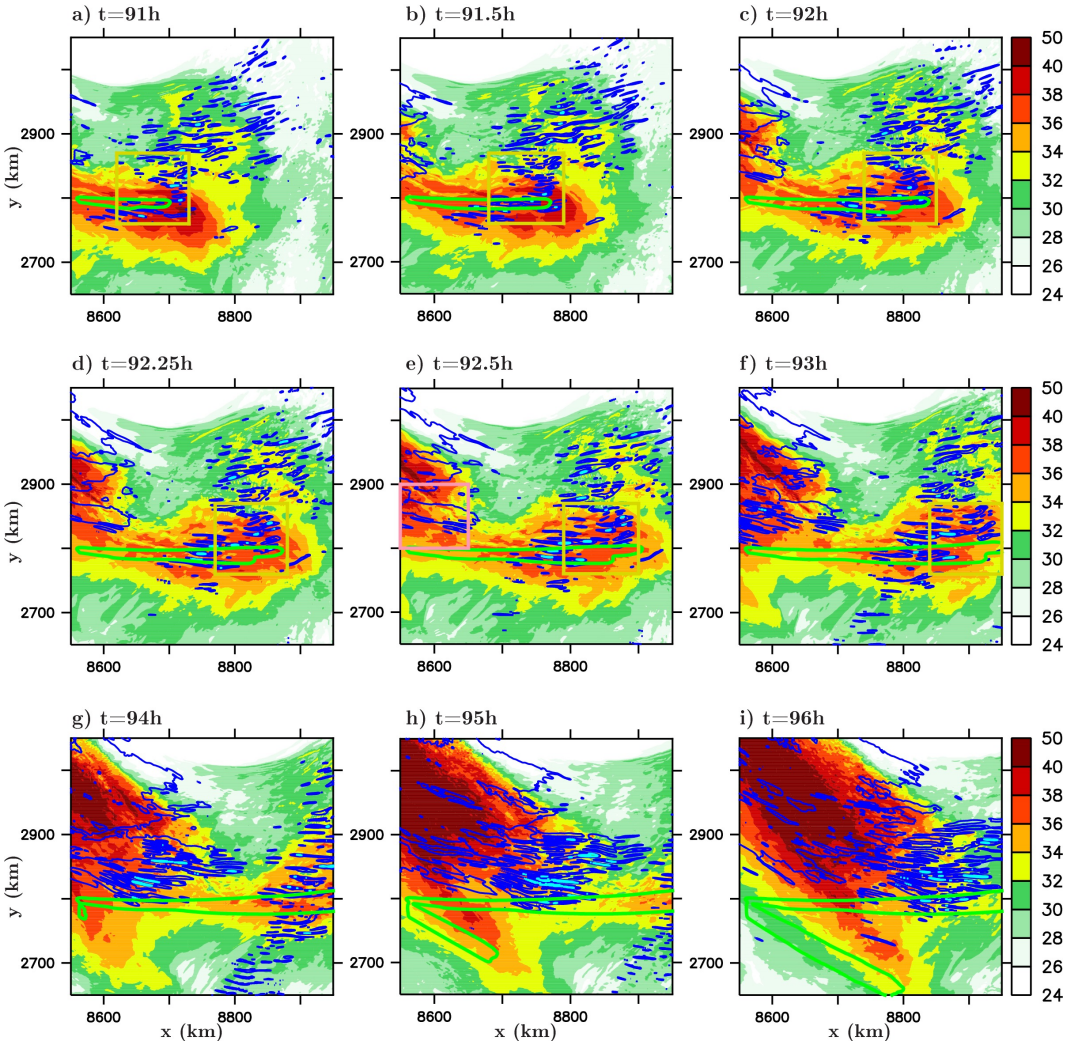

FIGURE 5 Horizontal wind speed at $z = 1.6$ km (shadings; units: m s^{-1}) and $z = 200$ m (28 and 30 m s^{-1} in blue contours and 32 m s^{-1} in light blue contours) at (a) $t = 91$ h, (b) $t = 91.5$ h, (c) $t = 92$ h, (d) $t = 92.25$ h, (e) $t = 92.5$ h, (f) $t = 93$ h, (g) $t = 94$ h, (h) $t = 95$ h, and (i) $t = 96$ h for S1land. The thick green contour corresponds to a given value of the passive tracer injected around $x = 8550$ km and $y = 2800$ km. The yellow squares are zoomed areas shown in Figure 6.

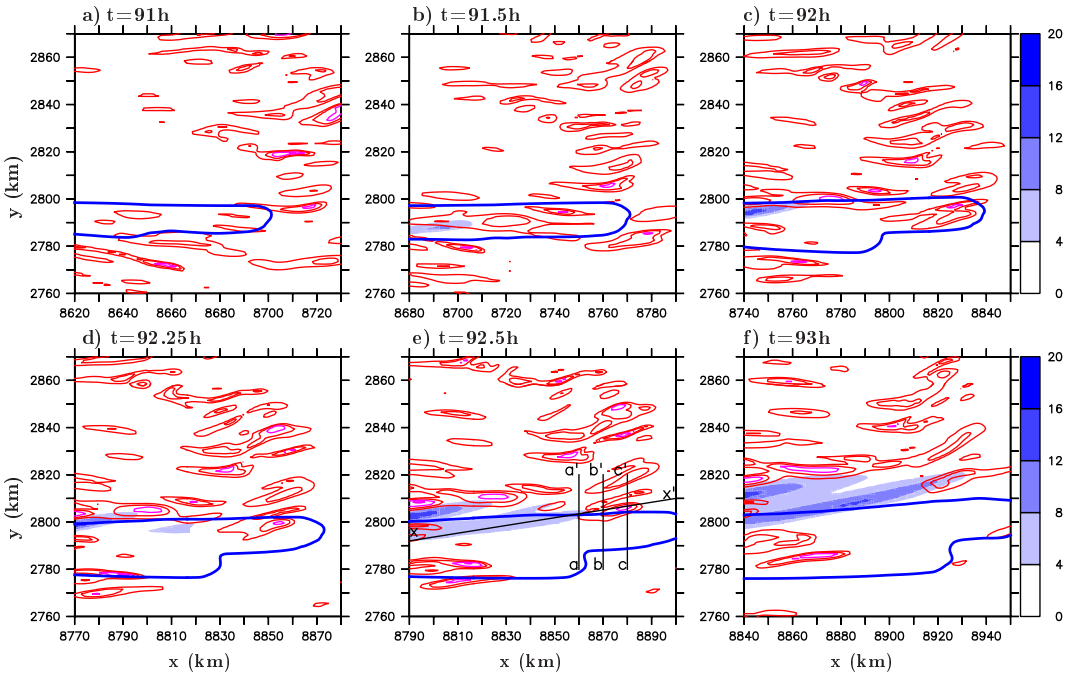

FIGURE 6 Passive tracer at $z = 500$ m (shadings) and $z = 1.6$ km (blue contour; value equals to 50), horizontal wind speed at $z = 200$ m (28 and 30 m s^{-1} in red contours and 32 m s^{-1} in magenta contours) at (a) $t = 91$ h, (b) $t = 91.5$ h, (c) $t = 92$ h, (d) $t = 92.25$ h, (e) $t = 92.5$ h and (f) $t = 93$ h for the zoomed areas shown in Figures 5(a)-(f).

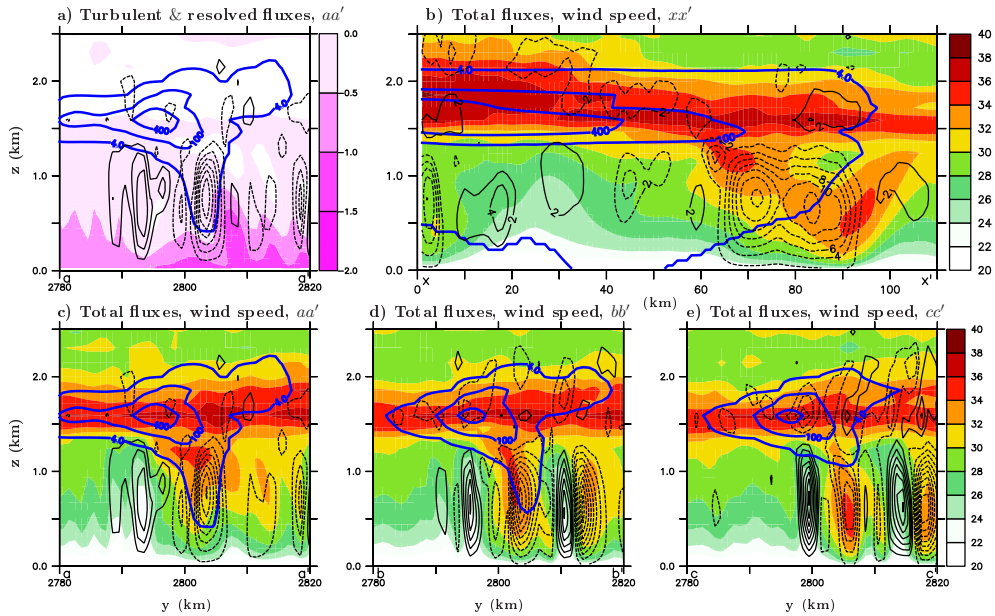

FIGURE 7 Vertical cross sections at $t = 92.5$ h shown in Figure 6(e). (a) cross section aa' of the vertical turbulent fluxes of zonal momentum (shadings; units: m^2s^{-2}), resolved vertical fluxes of zonal momentum (black dashed and solid contours for negative and positive values; interval: 2 m^2s^{-2}) and passive tracer (blue contour for a given value of 4). (b) cross section xx' of horizontal wind speed (shadings; units: m s^{-1}), total vertical fluxes of zonal momentum (black dashed and solid contours for negative and positive values; interval: 2 m^2s^{-2}) and passive tracer (blue contours for 4, 100 and 400 values). (c), (d) and (e) same as in (b) but for the cross sections aa', bb' and cc' respectively.

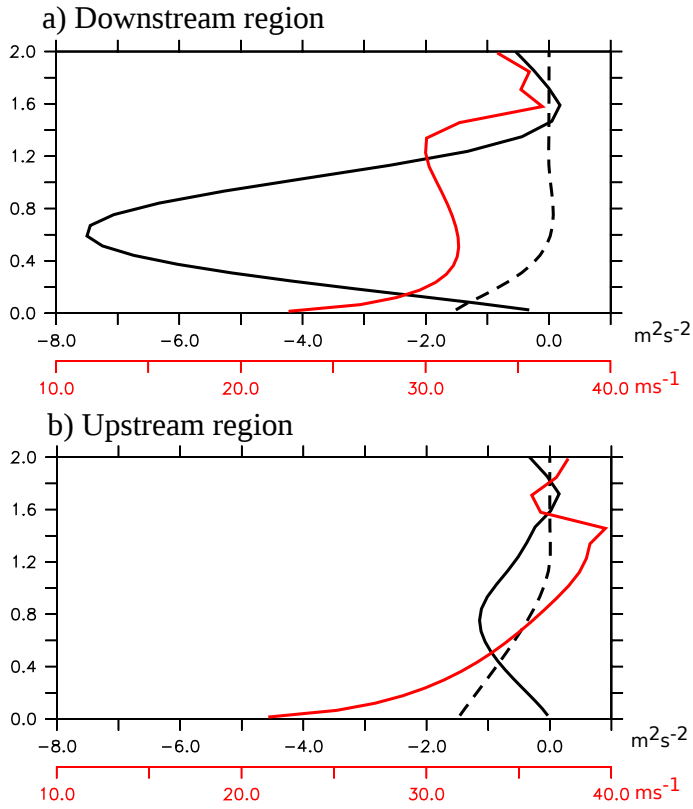

FIGURE 8 Vertical profiles of horizontal wind speed (red) and resolved (solid black) and turbulent (dash black) vertical fluxes of zonal momentum at $t = 92.5$ h in (a) downstream and (b) upstream regions shown respectively by the yellow and pink squares in Figure 5(e) where horizontal wind speed at $z = 200$ m exceeds 28 m s^{-1}.

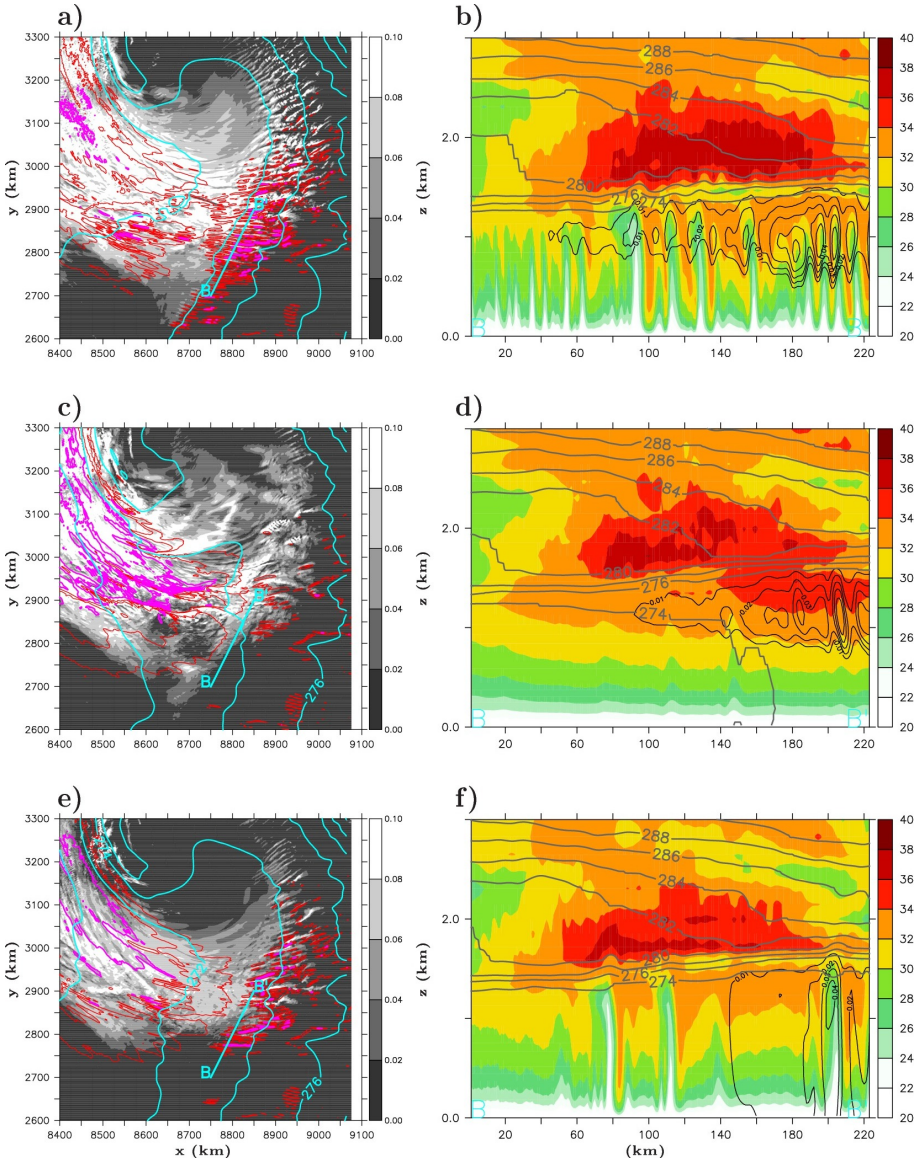

FIGURE 9 (Left column) Maximum of the sum of cloud liquid and ice water contents between $z = 0.0$ km and $z = 2.0$ km (grey shadings; units: g kg^{-1}), surface wind gusts (28 and 30 m s^{-1} in red contours and 32 and 34 m s^{-1} in magenta contours), and potential temperature at $z = 25$ m (light blue contours; interval: 2 K) at $t = 93$ h. The surface wind gusts is a linear function of the 10-m wind speed and the square root of the 10-m turbulent kinetic energy. The temperature field is spatially smoothed for clarity purposes. (Right column) Vertical cross sections BB' of the total precipitation (sum of snow, graupel and rain mixing ratios in black contours; int: 0.01 g kg^{-1}), horizontal wind speed (shadings; units: m s^{-1}), and potential temperature (grey contours: interval: 2K). (Upper panels) S1land, (middle panels) S1land_nocl, (lower panels) S1land_nocl_noevap.

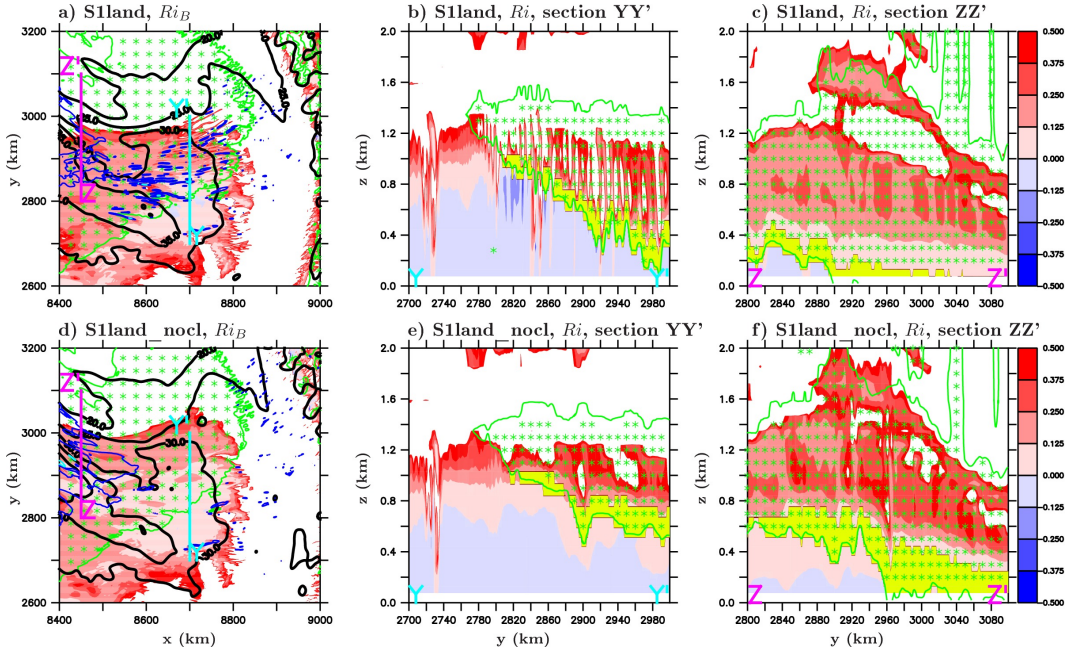

FIGURE 10 (a), (d) Bulk Richardson number computed between $z = 0.1$ km and $z = 1.2$ km (shadings), horizontal wind speed at $z = 1.6$ km (black contours; int: 5 m s^{-1} and a spatial smoothing is applied for clarity purposes) and $z = 200$ m (28 and 30 m s^{-1} in blue contours and 32 m s^{-1} in light blue contours), and ice water content (sum of cloud ice, snow and graupel) greater than 5 10^{-3} g kg^{-1} (green contours with asterisks). (b), (e) Vertical cross sections YY' of the Richardson number (shadings), ice water content (sum of cloud ice, snow and graupel) greater than 5 10^{-3} g kg^{-1} (green contours with asterisks). The yellow areas correspond to areas where CDI is satisfied. (c), (f) same as (b), (e) but for the cross section ZZ'. (Upper panels) S1land, (lower panels) S1land_nocl. All panels are computed at $t = 90$ h. Note that regions where the Richardson number exceeds 0.5 are in white.

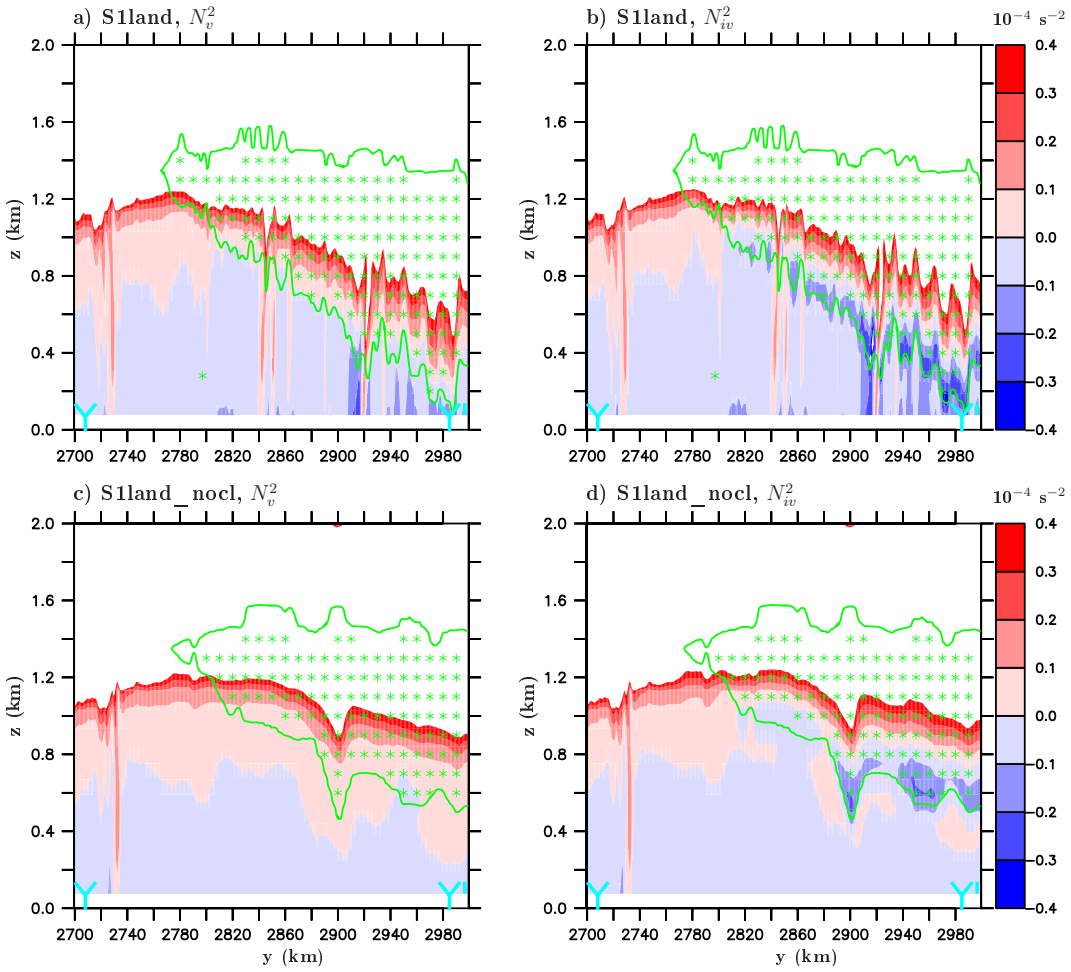

FIGURE 11 Vertical cross sections YY' of the square of the static stability (shadings; units: s^{-2}) for (a),(b) S1land and (c),(d) S1land_nocl at $t = 90$ h computed in two ways: (a), (c) $N_v^2 = (g/\theta_v)(\partial\theta_v/\partial z)$ and (b), (d) $N_{iv}^2 = (g/\theta_{iv})(\partial\theta_{iv}/\partial z)$. The ice water content (sum of cloud ice, snow and graupel) greater than 5 10^{-3} g kg^{-1} is represented in green contours with asterisks.

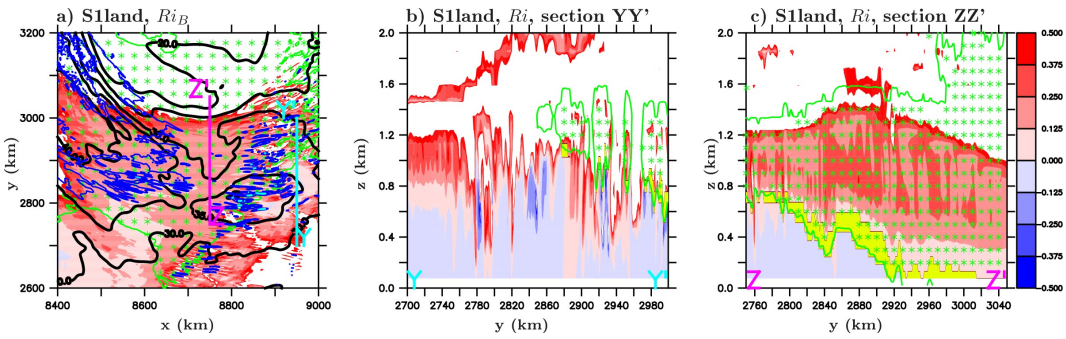

FIGURE 12 Same as Figures 10(a)-(c) but at $t = 93$ h.